Article

https://doi.org/10.1038/s41550-023-01966-2

Complete replacement of magnetic flux in a flux rope during a coronal mass ejection

Received: 29 September 2021

Accepted: 6 April 2023

Published online: 04 May 2023

Check for updates

Tingyu Gou[1], Rui Liu[1,2], Astrid M. Veronig[3], Bin Zhuang[4], Ting Li[5,6], Wensi Wang[1,7], Mengjiao Xu[1,8] & Yuming Wang[1,2,8]

Solar coronal mass ejections are the most energetic events in the Solar System. In their standard formation model, a magnetic flux rope builds up into a coronal mass ejection through magnetic reconnection that continually converts overlying, untwisted magnetic flux into twisted flux enveloping the pre-existing rope. However, only a minority of coronal mass ejections carry a coherent magnetic flux rope as their core structure, which casts doubt on the universality of this orderly wrapping process. Here we provide observational evidence of a different formation and eruption mechanism of a magnetic flux rope from an S-shaped thread, where its magnetic flux is fully replaced via flare reconnections. One of the footpoints of the sigmoidal feature slipped and expanded during the formation, and then moved to a completely new place, associated with the highly dynamical evolution of flare ribbons and a twofold increase in magnetic flux through the footpoint, during the eruption. Such a configuration is not predicted by standard formation models or numerical simulations and highlights the three-dimensional nature of magnetic reconnections between the flux rope and the surrounding magnetic field.

Magnetic flux ropes (MFRs), which consist of twisted magnetic field lines, play a key role in understanding various phenomena in astrophysical, space and laboratory plasmas. In solar physics, MFRs have been widely accepted as a fundamental structure in solar eruptions[1,2], which are accompanied by a rapid release of a huge amount of energy[3]. Driven by solar eruptions, space weather has become increasingly important for various technological systems in modern society[4], which makes it essential to study the genesis and eruptive mechanism of solar MFRs.

MFRs on the Sun manifest as various observational features, such as filaments, hot channels, coronal cavities and S-shaped loop bundles known as sigmoids[5–7]. A coherent MFR could either be present before the eruption[8,9] or form by magnetic reconnection within a sheared arcade during the eruption[10,11]. The two different scenarios, which refer to two competing pre-eruption magnetic field configurations of solar eruptions, that is, MFR versus sheared magnetic arcade[1], have been attracting great interest and have been under intense debate for decades. Recent observations reveal that a coherent MFR may build up on a core 'seed' that is initiated from the coalescence of mini-plasmoids in a pre-existing current sheet[12], which gives a specific intermediate state between the two distinct configurations, that is, a 'hybrid' state with a twisted core embedded in a sheared arcade[2].

The standard flare model describes the eruption of a pre-existing MFR, in which magnetic reconnection in the current sheet underneath adds field lines wrapping around the rising rope[13,14], producing post-flare loops connecting two parallel flare ribbons on the surface. In consideration of three-dimensional (3D) reconnection occurring

[1]School of Earth and Space Sciences/CAS Center for Excellence in Comparative Planetology/CAS Key Laboratory of Geospace Environment, University of Science and Technology of China, Hefei, China. [2]Collaborative Innovation Center of Astronautical Science and Technology, Hefei, China. [3]Institute of Physics & Kanzelhöhe Observatory for Solar and Environmental Research, University of Graz, Graz, Austria. [4]Institute for the Study of Earth, Oceans, and Space, University of New Hampshire, Durham, NH, USA. [5]CAS Key Laboratory of Solar Activity, National Astronomical Observatories, Beijing, China. [6]School of Astronomy and Space Science, University of Chinese Academy of Sciences, Beijing, China. [7]Mengcheng National Geophysical Observatory, University of Science and Technology of China, Mengcheng, China. [8]Deep Space Exploration Laboratory, Hefei, China. e-mail: tygou@ustc.edu.cn; rliu@ustc.edu.cn

https://doi.org/10.1038/s41550-023-01966-2

at quasi-separatrix layers (QSLs) that separate the MFR from the surrounding untwisted fields[15], the two-dimensional (2D) standard model is extended to three dimensions, with the (quasi-)separatrix footprints of coronal magnetic fields mapped by double J-shaped flare ribbons[16–18]: the straight sections of flare ribbons correspond to the footprints of the hyperbolic flux tube (a collection of two intersecting QSLs[19]) below the MFR, which is the 3D counterpart of the vertical current sheet in the 2D model; the endmost hooks correspond to the footprints of the QSLs wrapping around the MFR, thus outlining its two feet anchored in the dense photosphere. Inside the hooks, coronal emission dims due to the evacuation of coronal matter along the rope's legs during the eruption[20–23]. Thus motions and morphological changes of flare ribbons, as the chromospheric imprint of coronal reconnections, reflect the changes of coronal magnetic connectivities and the evolution of eruptive MFRs.

After solar eruptions, MFRs are sometimes detected in situ in interplanetary space and termed magnetic clouds, which are characterized by a large and smooth rotation in the field's direction, enhanced magnetic field strength, a depressed proton temperature and density, and a low plasma β (refs. 24,25). However, only about one-third of interplanetary coronal mass ejections (CMEs) possess typical MFR features[26], in spite of their same origin from the Sun. This mismatch between the in situ observation and the anticipation that all CMEs are essentially MFRs[27] is traditionally attributed to interactions among the ejecta and the solar wind as well as to unfavourable spacecraft trajectories within ejecta[28], but are there also other physical mechanisms that can account for some of the absence of well structured MFRs that manifest as complex ejecta in interplanetary space?

Here we study the formation and eruption of a solar MFR in a sigmoidal active region. The combination of the low-atmosphere and coronal observations highlights the buildup of an MFR before the eruption and its subsequent restructuring during the eruption. The lower-atmosphere counterpart of the erupting structure exhibits a highly dynamic evolution while one of its feet migrates to a completely new location compared with the pre-eruption MFR, which indicates a complete replacement of magnetic fluxes in the rope. The restructuring of the MFR highlights the importance of 3D reconnections with the surrounding coronal magnetic fields during its development into a CME, and sheds light on the implication of the complex dynamics occurring in the solar source active region for interplanetary ejecta.

Results

Overview of the event

The eruption of interest occurred in the National Oceanic and Atmospheric Administration active region 12158 on 2014 September 10 near the solar disk centre. The active region consists of a leading positive-polarity sunspot surrounded by negative polarities in the southeast, and it exhibits a typical sigmoidal configuration (Fig. 1 and Supplementary Video 1). A bundle of inverse-S-shaped loops was observed several hours before the eruption in the Solar Dynamics Observatory (SDO)/Atmospheric Imaging Assembly (AIA) (Methods) 94 Å channel (Fig. 1d and Supplementary Video 2). The eruption starts with the rise of a coherent sigmoidal structure as observed in AIA's hot passbands (for example, 131 Å; Fig. 1b and Supplementary Video 1), which was interpreted as an MFR in previous studies on the event[29–31]. It produces a Geostationary Operational Environmental Satellite (GOES) X1.6-class (Methods) flare starting at 17:21 UT, and a fast halo CME, which is detected as an interplanetary CME near the Earth two days later (Supplementary Note 1.3).

A sigmoidal MFR builds up from a thin thread in the core of a sheared magnetic arcade during the flare precursor phase (Fig. 1a,b), accompanied by footpoint brightening in the low solar atmosphere. The western foot of the pre-eruption MFR is located in positive polarities near the sunspot (Fig. 1g); the eastern foot in negative polarities is outlined by a low-atmosphere ribbon-like brightening (Fig. 1b,e). During the eruption, the same ribbon undergoes rapid and complex changes (Fig. 1c,f–h). Below we study in detail the formation of the sigmoid and its complex evolution during the eruption.

Appearance of the seed MFR

The eruptive sigmoid originally appears as a brightening inverse-S-shaped thread in SDO/AIA 131 Å at ~16:45 UT (Figs. 2 and 3), when the GOES 1–8 Å flux starts to rise slowly (Fig. 4a). The brightening thread is co-spatial with a low-lying filament (Fig. 2d), which remains almost unperturbed during the MFR eruption (Extended Data Fig. 1 and Supplementary Note 1.2). The filament is aligned along the main polarity inversion line (PIL) of the active region, where a number of bald-patch (BP) candidates are identified (Fig. 2f and Methods). Embedded in a bundle of sheared sigmoidal loops observed in AIA 94 Å (Fig. 2c) and almost invisible in other cool AIA channels such as 211, 193 and 171 Å, the S-shaped thread has a mean temperature of about 7 MK with a dominant hot emission measure (EM) component at $\log T \approx 6.7$–7.0, where T is the temperature, according to the differential emission measure (DEM) distribution sampled on the thread (labelled S in Fig. 3; Methods). The EM locus curves of six extreme-ultraviolet (EUV) channels from the thread form an envelope over the multipeak DEM distribution (Fig. 3b and Methods), corroborating the DEM result. The reference DEM distribution sampled from a nearby region off the thread (labelled R in Fig. 3) shows similar cool EM components at $\log T \approx 5.5$–6.6 but much weaker EMs at $\log T \approx 6.7$–7.0, confirming the presence of hot plasmas in the thread. The newly appeared hot thread is later observed to continually grow into the eruptive sigmoid, and hence is termed a seed MFR hereafter[2,12].

Buildup of the MFR

As soon as it appears, the seed MFR further extends the 'elbows' of the inverse-S shape and grows thicker (Extended Data Fig. 2 and Supplementary Video 3) from a few megametres to ~30 Mm within the next ~35 min before the eruption, as can be seen in the stack plot made from the virtual slit S1 across the sigmoid (Fig. 4c, Extended Data Fig. 2a and Methods). The growth of the seed MFR is associated with a slow rise in the GOES 1–8 Å soft X-ray flux (Fig. 4a), before the onset of intense energy release at ~17:21 UT. DEM analysis evidences intense heating during the formation of the MFR (Extended Data Fig. 3 and Supplementary Note 1.1).

With the development of the MFR, notable pre-flare ribbon brightenings in the low atmosphere are observed with both SDO/AIA and the Interface Region Imaging Spectrograph (IRIS) (Extended Data Fig. 2 and Supplementary Video 3). As the seed MFR extends to form a complete inverse-S shape, a trapezoid-shaped ribbon is spawned from the far end of the eastern ribbon (Extended Data Fig. 2). The spawning process is demonstrated in the stack plots of the virtual slits S2 and S3 (Fig. 4d,e, Extended Data Fig. 2d and Methods). The trapezoidal ribbon shows a fast and then slow expansion, which is associated with the fast and then slow widening of the coherent sigmoid observed in AIA 131 Å (Fig. 4c–e). Comparing AIA 131 Å and IRIS 1,400 Å images at about 17:12 UT (Fig. 5a,d and Extended Data Fig. 2), we can see that the trapezoidal ribbon is the footpoints of coronal loops belonging to the sigmoidal MFR. That the expansion of the trapezoidal ribbon is accompanied by the sigmoid thickening argues strongly for the development of a twisted MFR[21,32]. During this phase, the instantaneous slipping motion proceeds almost perpendicularly to the overall direction of the ribbon extension, which is described as 'squirming' motion in a previous study[30]. During the flare precursor phase, the rate of the magnetic reconnection that contributes to the MFR buildup is estimated to vary around 2×10^{19} Mx s^{-1} (Fig. 4b and Methods), a few times lower than, but still of the same magnitude as, that during the MFR eruption.

 https://doi.org/10.1038/s41550-023-01966-2

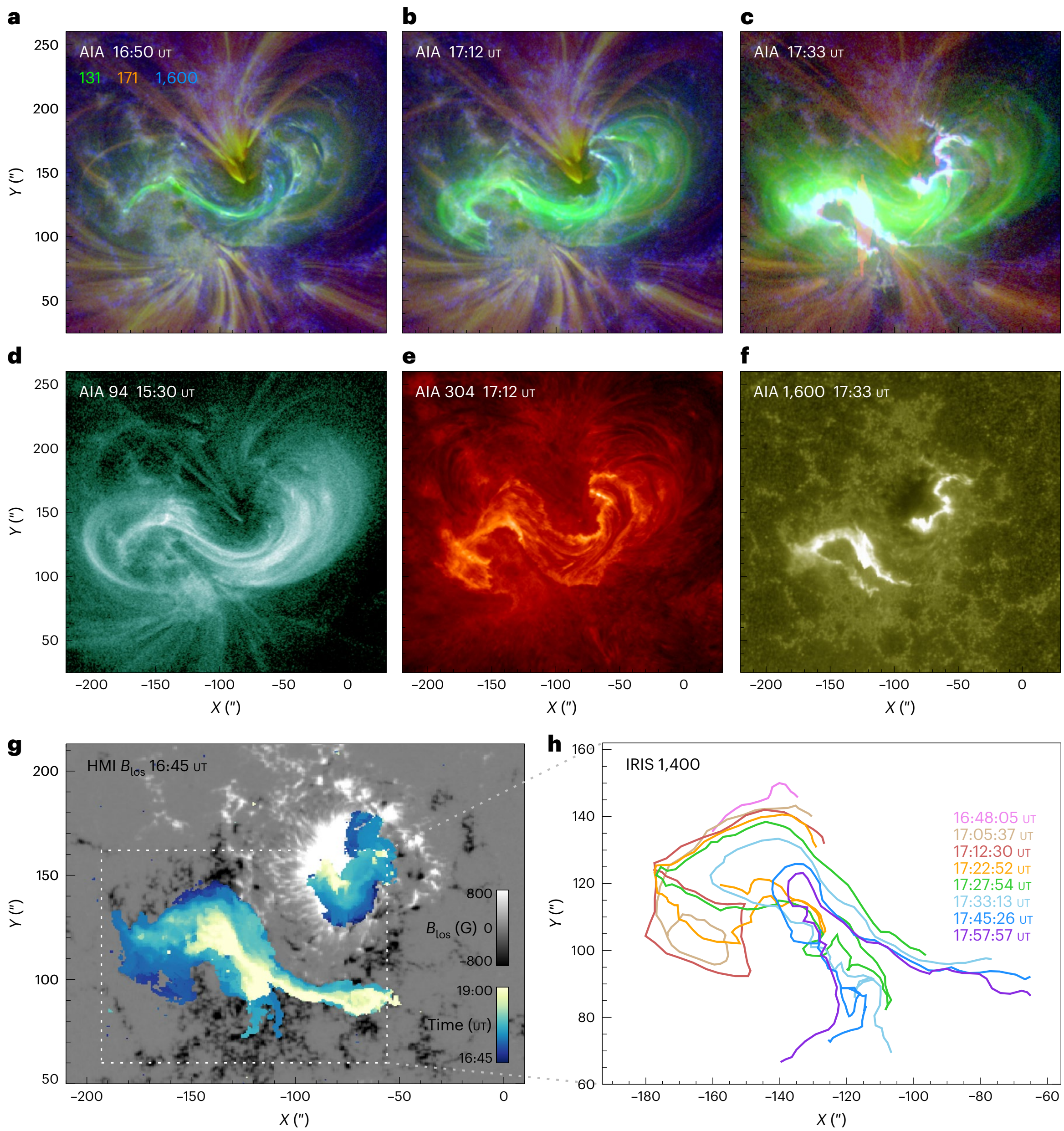

Fig. 1 | Overview of 2014 September 10 sigmoid event. a–**c**, SDO/AIA 131 Å (green), 171 Å (orange) and 1,600 Å (blue) composite images during different evolutionary phases, showing the seed MFR beneath large-scale active-region loops (**a**), the coherent sigmoidal MFR before eruption (**b**) and post-flare loops and flare ribbons after the eruption (**c**) **d**, SDO/AIA 94 Å image about two hours before the eruption, showing sheared inverse-S-shaped loops. **e**, SDO/AIA 304 Å image observed at the same time as **b**, showing the trapezoid-shaped ribbon co-spatial with the eastern foot of the sigmoid. **f**, SDO/AIA 1,600 Å image observed at the same time as **c**, featuring the flare ribbon during the eruption. **g**, SDO/Helioseismic and Magnetic Imager (HMI) line-of-sight magnetogram before the flare, superposed by colour-coded temporal evolution of ribbon brightenings identified in AIA UV passbands (Methods). B_{los}, line-of-sight magnetic field. **h**, A schematic zooming in on representative ribbon fronts in negative polarities, which are manually traced from IRIS SJI 1,400 Å images at selected time instants (Methods).

Ribbon evolution during eruption

Shortly after being well developed, the MFR erupts to produce an intense X-class flare. The flare ribbon in the positive-polarity region (PR) remains relatively stationary (Fig. 1g and Extended Data Fig. 4b), probably due to its proximity to the sunspot where the strong magnetic field is relatively 'rigid'; the ribbon in the negative-polarity region (NR), which is associated with the eastern foot of the MFR, evolves greatly and rapidly during the eruption (Fig. 1g,h, Extended Data Fig. 4 and Supplementary Video 3).

From about 17:18 UT, NR's hook changes from a closed to an open morphology (Fig. 5, Extended Data Fig. 4 and Supplementary Video 3). As the ribbon moves, it sweeps the trapezoidal ribbon that encloses the eastern foot of the pre-eruption MFR. During the eruption, both ends of NR elongate rapidly southwestwards, and the whole ribbon develops into a horseshoe shape (Extended Data Fig. 4). The northern branch of NR (NR_n), which host negative footpoints of post-flare loops, extends rapidly along the direction of the main PIL; the motion is associated with the strong-to-weak shear transition of the post-flare arcade observed in AIA (Extended Data Fig. 4 and Supplementary Video 3). Sometimes NR_n itself shows two parallel branches in IRIS 1,400 Å (for example, at 17:33 UT; Extended Data Fig. 4d), but they are not resolved in AIA 1,600 Å observations. The southern part of the horseshoe-shaped

https://doi.org/10.1038/s41550-023-01966-2

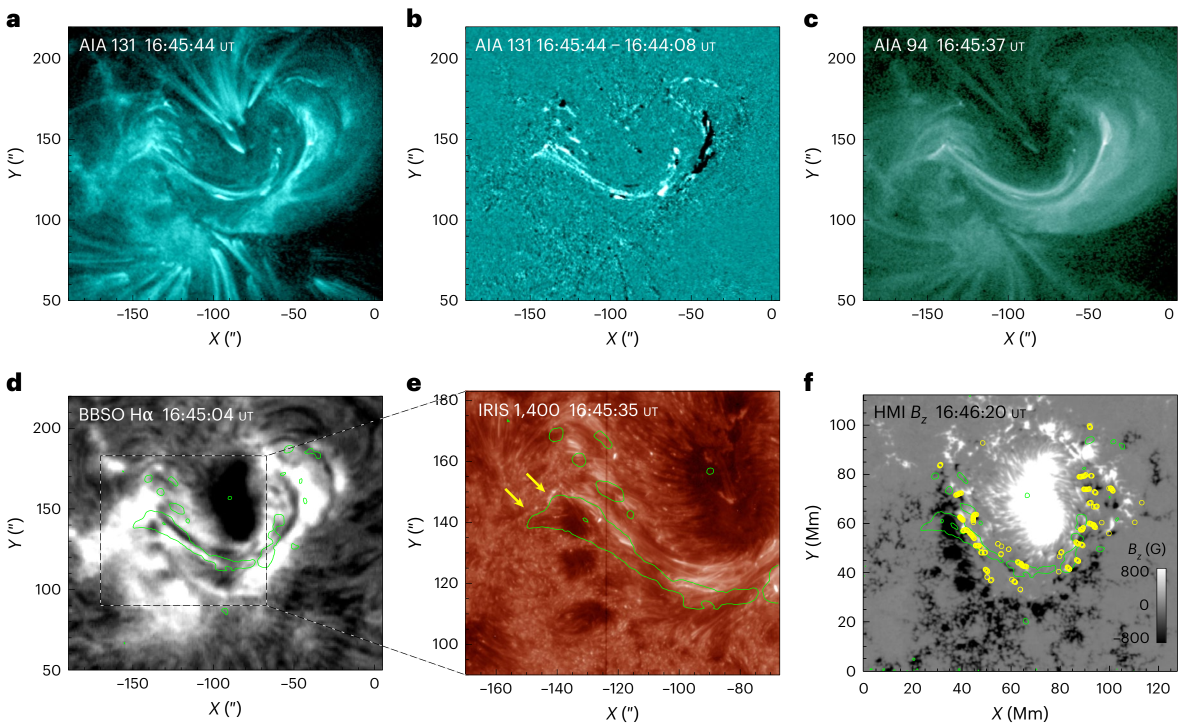

Fig. 2 | Appearance of the seed MFR at 16:45 UT. **a**–**c**, SDO/AIA 131 Å (**a**), difference (**b**) and 94 Å (**c**) images, featuring the S-shaped thread beneath the sheared arcade. **d**,**e**, Big Bear Solar Observatory (BBSO) Hα line centre (**d**) and IRIS SJI 1,400 Å (**e**) images. The dotted rectangle in **d** indicates the field of view (FOV) of **e**. Green contours superimposed in **d**,**e** are taken from the S-shaped thread observed in AIA 131 Å. Yellow arrows in **e** mark the IRIS 1,400 Å brightenings associated with the appearance of the S-shaped thread in AIA 131 Å. **f**, SDO/HMI space-weather HMI active-region patch (SHARP) B_z map with cylindrical equal area (CEA) projection. B_z refers to the vertical magnetic field component. Yellow symbols indicate BP candidates at the PIL of the active region (Methods). Superimposed green contours are the same as in **d**,**e** except for being remapped with CEA projection.

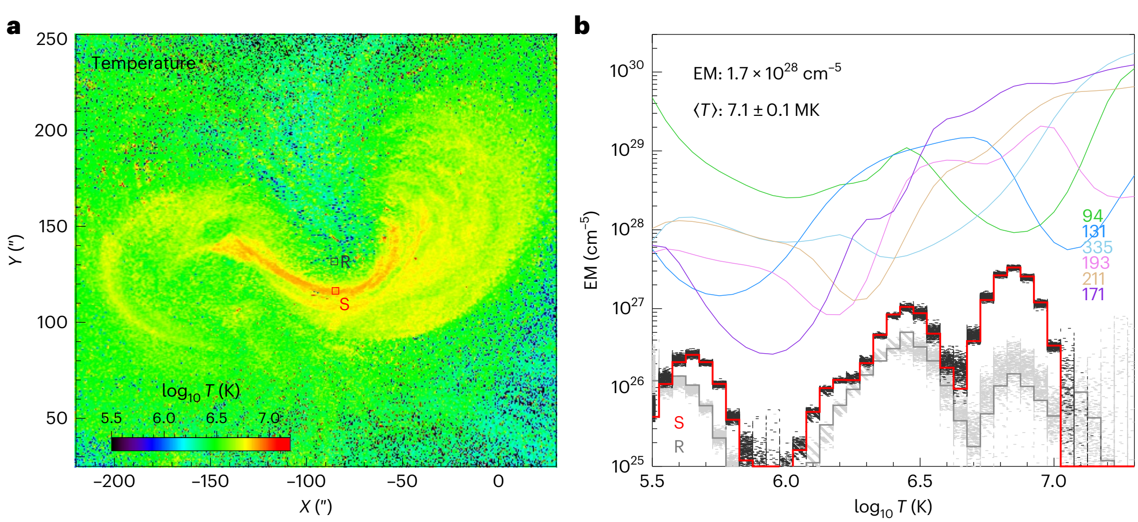

Fig. 3 | Temperature structure of the seed MFR. **a**, Map of DEM-weighted mean temperature as scaled by the colour bar (Methods). **b**, EM locus curves of six AIA EUV channels (coloured lines; Methods) and DEM distribution (the thick red curve) sampled from a region (4 × 4 $pixel^2$) on the S-shaped thread (indicated by the red box S in **a**). The reference DEM distribution from a nearby region (R in **a**) is shown by the thick grey curve. Black and light-grey curves give their Monte Carlo simulations (Methods). Annotated are the total EM and mean temperature of the thread sample S.

ribbon (NR_s) completes the hooked part of NR, which supposedly maps the footprint of the QSLs that wrap around the erupting MFR[20].

In particular, NR_s exhibits irregular, complex motions (Fig. 1h and Supplementary Video 3). It zigzags towards the southwest, in a serpentine fashion. The stack plot of the virtual slit S4 across the horseshoe-shaped ribbon (Extended Data Fig. 4d) nicely shows the zigzag motions of NR_s, which leave irregular trails, distinct from the rather smooth track left by NR_n (Fig. 4f). As the eruption proceeds, the horseshoe shape is stretched, but its opening becomes wider, and here coronal dimmings develop (Fig. 5 and Extended Data Fig. 4).

https://doi.org/10.1038/s41550-023-01966-2

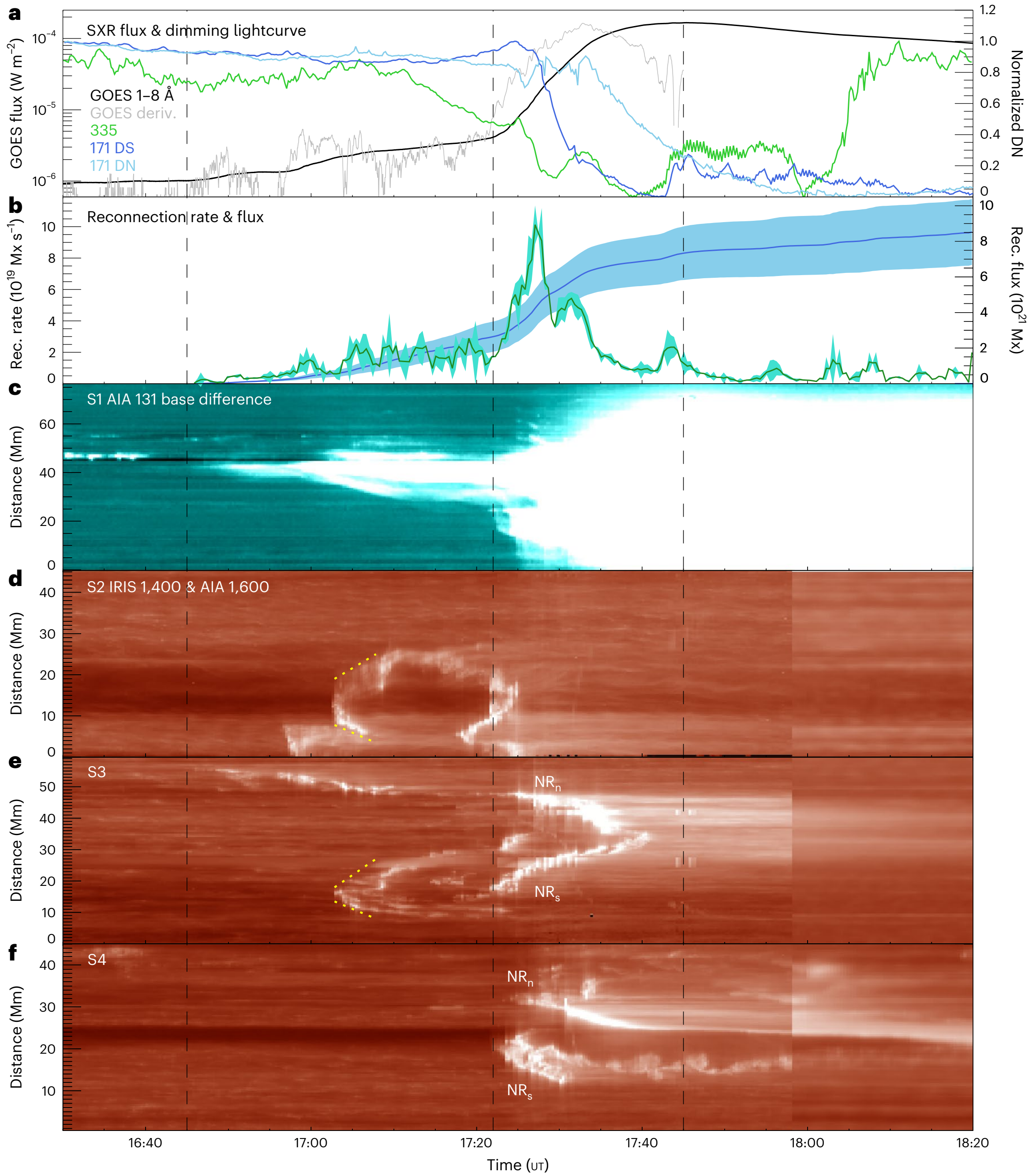

Fig. 4 | Temporal evolution of the event. a, GOES 1–8 Å soft X-ray (SXR) flux (black solid line; scaled by the left *y* axis), its time derivative (grey line; scaled by an arbitrary *y* axis) and normalized dimming lightcurves obtained from AIA 335 Å and 171 Å (coloured lines; scaled by the right *y* axis; Methods). 'DN' and 'DS' indicate the sampled north and south dimming regions, respectively (marked in Extended Data Fig. 6d). **b**, Magnetic reconnection rate (green; scaled by the left *y* axis) and the accumulative reconnection flux (blue; scaled by the right *y* axis; Methods). Light green and blue shaded areas are corresponding uncertainties. **c**–**f**, Stack plots made from four virtual slits, S1–S4 respectively, as denoted in Extended Data Figs. 2 and 4 (Methods). Yellow dotted lines in **d**,**e** mark the tracks left by the fast expansion of the trapezoidal ribbon. NR$_n$ and NR$_s$ in **e**, **f** mark the tracks left by the two branches of the negative ribbon (Extended Data Fig. 4d). The three vertical dashed lines mark successively when the seed MFR appears (16:45 UT) and when the GOES X1.6-class flare starts (17:21 UT) and peaks (17:45 UT).

During the flare decay phase, NR$_s$ fades away, and only NR$_n$ remains visible in AIA 1,600 Å images (Figs. 1g and 4f). During the eruption, some bright knots are observed to distribute quasiperiodically and move along the ribbon, which may indicate that the slipping reconnection proceeds quasiperiodically[33].

The ribbon brightening in IRIS Slit-Jaw Imager (SJI) 1,400 Å images shows three phases of temporal evolution (Fig. 6), that is, (1) the development of the trapezoidal ribbon from 16:45 to 17:18 UT, (2) the change of NR's hook from a closed to an open morphology from 17:18 to 17:26 UT and (3) the evolution of the horseshoe-shaped NR afterwards. It is remarkable that most of the region enclosed by the trapezoidal ribbon (marked by orange dotted lines in Fig. 6) that is swept during the first phase is swept again during the second phase (as shown in blue in Fig. 6d), which suggests that the reconnections taking place during

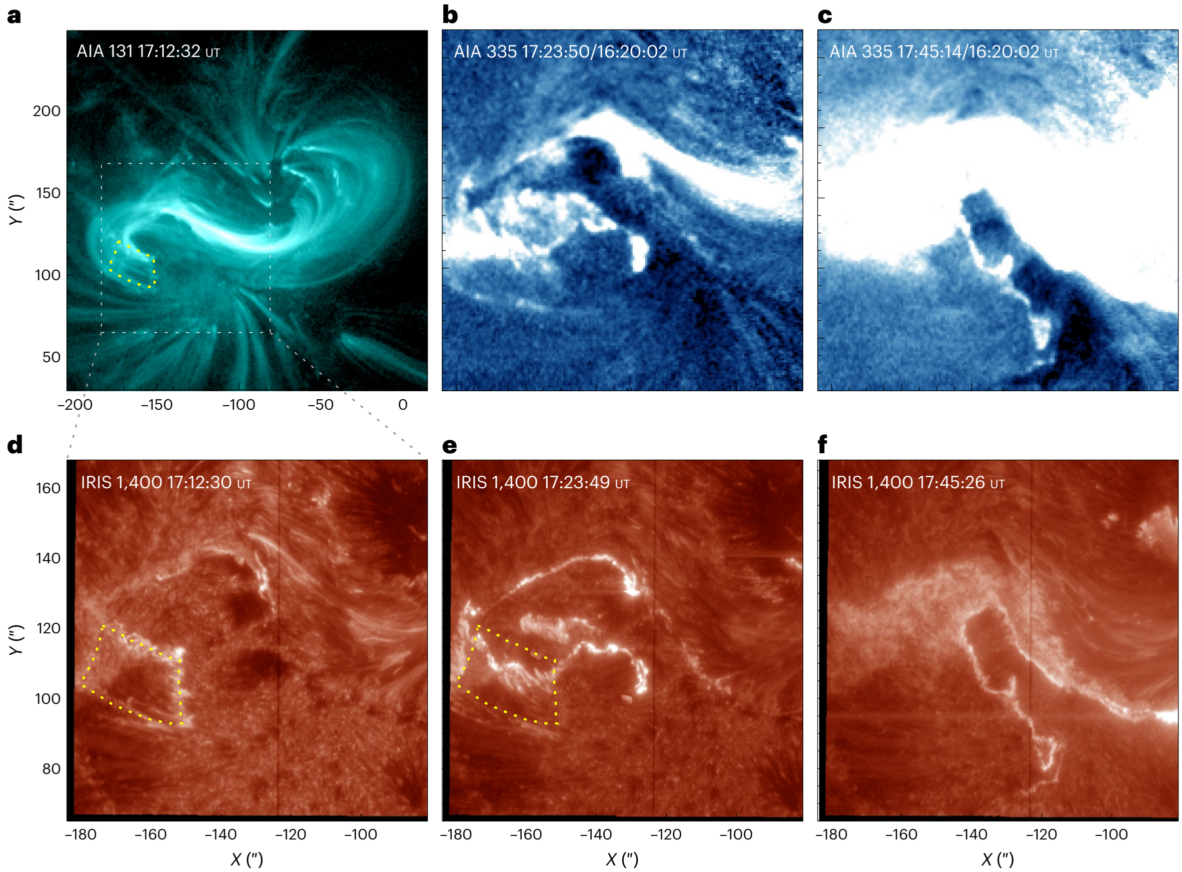

Fig. 5 | Footpoint migration during the MFR eruption. a, SDO/AIA 131 Å observation showing the pre-eruption sigmoid. The white dotted rectangle indicates the zoom-in FOV of **b**–**f**. **b**,**c**, SDO/AIA 335 Å base-ratio images featuring the coronal dimming during the flux-rope eruption. **d**–**f**, IRIS SJI 1,400 Å images observed at the same time as the AIA images in **a**–**c**, respectively, showing the dynamic evolution of the flare ribbon. The yellow dotted lines in **a**,**d**,**e** denote the location of the trapezoidal ribbon in **d** (see also Extended Data Figs. 2 and 4), which is co-spatial with the eastern foot of the sigmoid in **a**.

the second phase must have involved most of the magnetic flux in the MFR formed during the first phase. It is also remarkable that NR_n, the ribbon segment that hosts the negative footpoints of flare loops, only appears during the third phase (Fig. 6c,d). In contrast, in a different event featuring an MFR under formation during the eruption[21], the two straight flare ribbons appear first and later extend and develop a closed hook at the far end of each ribbon, enclosing the rope's two feet.

Association with coronal dimming

Enclosed by flare ribbons, two dimming regions are observed in cool AIA EUV passbands (Extended Data Fig. 5), indicative of coronal mass loss along two feet of the CME. The dimming in negative polarities as enclosed by NR is evident in AIA 335 Å images, and it migrates as the MFR erupts (Fig. 5b,c, Extended Data Fig. 4c and Supplementary Video 4). The dimming lightcurve (Fig. 4a and Methods) shows that coronal dimming around NR starts to develop from ~17:10 UT onward, when the MFR is well developed, as characterized by its eastern foot being fully outlined by a trapezoidal ribbon. However, the initial dimming is not enclosed by, but located outside, the trapezoid (Fig. 6e and Methods). During the eruption, in spite of strong diffraction patterns in AIA images, the dimming intensifies, as shown by the 335 Å lightcurve (Fig. 4a). The coronal dimming occupies a position mainly within the horseshoe-shaped ribbon, close to the NR_s side (Fig. 6f,g). As the horseshoe shape of NR is stretched, the dimming region is mainly concentrated in the opening of the horseshoe after 17:50 UT (Fig. 6h), and it remains quasistationary thereafter during the long-duration decay phase (Supplementary Video 4). A conjugated pair of dimmings is identified on both the northern and southern sides of the post-flare arcade during the late decay phase (Extended Data Fig. 6). Corresponding to the extended decreasing brightness (Fig. 4a and Methods), these dimmings continue to map the two footpoints of the CME, whose connection settles in the north–south direction (Extended Data Fig. 6d), in contrast to the orientation of the pre-eruption MFR, which is mainly along the east–west direction (Extended Data Fig. 6a).

Combining the evolution of flare ribbon and coronal dimming (Fig. 6), we conclude that the eastern foot of the MFR undergoes a marked migration during the eruption. The centroid of magnetic fluxes through the foot is shifted by about 70″ during the impulsive eruption (Fig. 6h and Methods). Its average migrating speed is about 26 km s^{-1}, substantially faster than the typical Alfvén speed in the lower solar atmosphere (~10 km s^{-1}) and the typical speed of photospheric flows (~1 km s^{-1}). Considering the irregular and highly dynamic motions of the ribbon hook (Fig. 1h and Supplementary Video 3), the instantaneous migration speed would also be irregular and most likely bursty. The magnetic flux through the foot, which gives an estimation of the toroidal flux of the rope, increases from about 3.3×10^{20} Mx to 7.9×10^{20} Mx during the flare impulsive phase (Methods). Thus, the substantial displacement of and the associated twofold increase in magnetic flux through the foot strongly evidence a complete restructuring of the original MFR during its development into the CME. This is radically different from the continuous deformation and drifting of flux-rope footpoints found in previous studies[34,35].

Discussion

To summarize, we investigated the formation and eruption of a sigmoidal MFR with coronal EUV and low-atmosphere UV observations.

https://doi.org/10.1038/s41550-023-01966-2

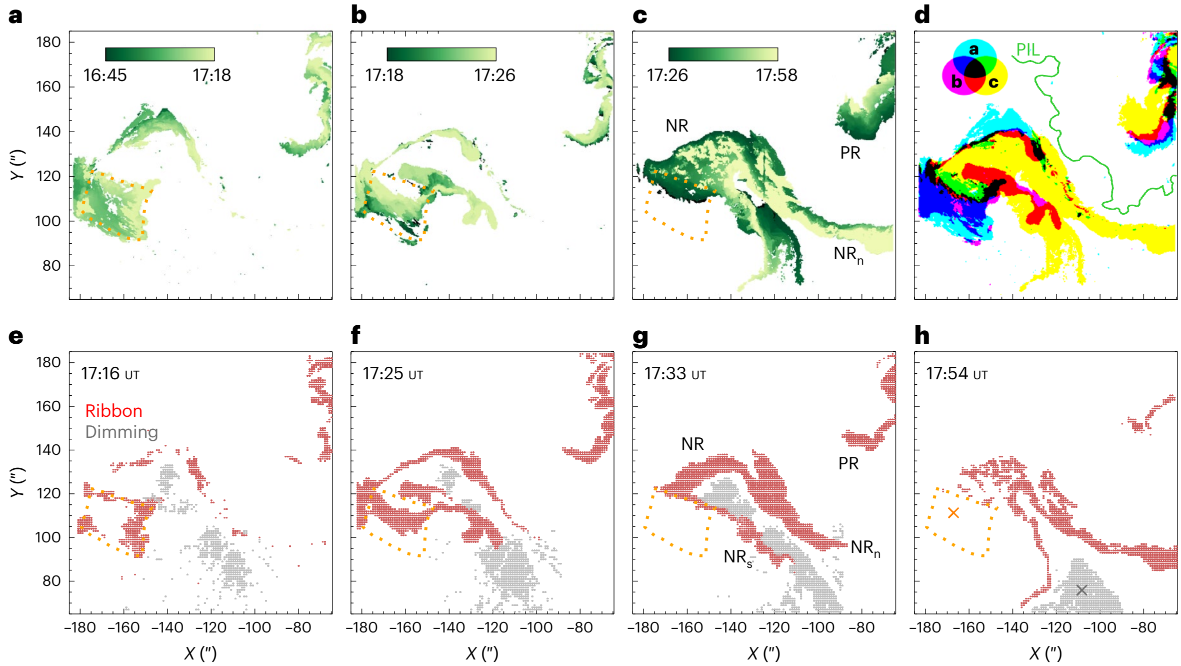

Fig. 6 | Evolution of flare ribbons in relation to coronal dimmings. a–c, Colour-coded temporal evolution of the ribbon brightening as identified in IRIS SJI 1,400 Å during three successive time intervals (Methods). **d**, Synthesized ribbons from **a**–**c**. The ribbon-swept region in each individual time interval is marked by cyan, magenta and yellow colours, respectively. Regions that are swept over more than once, that is, by ribbons developed in different time intervals, are hence shown in blended colours. The green curve shows the main PIL of the active region. **e**–**h**, Snapshots of IRIS SJI 1,400 Å ribbon and SDO/AIA 335 Å dimming, which are obtained by summing up brightened and dimmed pixels over a ~1 min interval around the specified time instants, respectively. Dotted orange lines denote the trapezoidal ribbon in **a**. The orange and grey crosses in **h** indicate the centroids of magnetic fluxes in the trapezoidal ribbon and in the dimming region, respectively (Methods).

We observe that the coherent sigmoid builds up on a slim S-shaped seed loop beneath a sheared arcade within tens of minutes during the flare precursor phase (Fig. 2 and Extended Data Fig. 2). The buildup process features not only the lengthening and thickening of the S-shaped seed in the AIA 131 Å passband, but also its eastern footpoint slipping away from the core field and subsequently expanding into being enclosed by a trapezoidal ribbon in IRIS SJI 1,400 Å, which argues strongly for the development of a twisted MFR. During the eruption, the trapezoidal ribbon transforms into an open hooked one. However, the open hooked region has little overlap with the original trapezoidal region (Figs. 5 and 6), indicating that the eastern foot of the pre-existing MFR undergoes a marked migration, which is associated with a twofold increase in magnetic flux through the rope's foot. These observations substantiate a complete replacement of magnetic fluxes in the original MFR by flare reconnections during the impulsive phase.

During the eruption, the ribbon hook NR$_s$, which maps the footprints of the MFR's QSL boundary, exhibits complex patterns and evolves dynamically (Fig. 1h and Supplementary Video 3). This suggests that complicated reconnections take place at the coronal QSLs, such as between the MFR and the overlying arcade or within the MFR itself[34,36,37]. The zigzag motions of NR$_s$ and repetitive brightenings at some locations inside the hook (Fig. 6 and Supplementary Video 3), which are often associated with rapid changes of the hook shape (Fig. 1h), suggest that there is an intense competition between the reconnections that turn the arcade field (anchored outside the hook) into the rope field (anchored inside the hook) and those that turn the rope field back into the (post-flare) arcade field[34,35]. The former reconnections build up the MFR, but the latter has the potential of eroding[34] or even disintegrating the original MFR. In our case, the former reconnections dominate over the latter, as indicated by the twofold increase of magnetic flux through the rope, but their competition drives the migration of the pre-eruption MFR's eastern foot to a completely new place during the eruption (Fig. 6).

The peak reconnection rate during the eruption is as high as ~1.0×10^{20} Mx s^{-1} (Fig. 4b and Methods). In comparison with the toroidal flux through the flux rope, which is of the order of 10^{20} Mx, the total reconnected flux is about 9.5×10^{21} Mx (Methods; until 19:00 UT during the flare decay phase), which falls into the top ~5% of poloidal fluxes of magnetic clouds in statistical studies[38,39]. In addition, the total reconnected flux during the flare is as high as ~66% of the unsigned magnetic fluxes in the active region, in the context of statistical results showing that no more than 50% of the total active-region flux is involved in the largest flares[40,41].

This on-disk sigmoid event provides a top view of a sigmoid growing continually from a hot inverse-S-shaped thread (Extended Data Fig. 2), which complements the side view of a limb eruption in a previous study[12] to substantiate the scenario that a large-scale MFR may build up from a small-scale seed rope, with the seed formation marking the sudden commencement of the transition from a sheared arcade to a CME MFR[2,12,42] (Supplementary Note 1.1). Since the footpoints of the pre-eruption MFR are distinct from those of the CME (Fig. 6 and Extended Data Fig. 6), the eruptive scenario is different from the standard picture, in which flare reconnections build up a pre-existing MFR by turning untwisted arcade field lines into twisted field lines wrapping around the rope[14,16,18]. In contrast, flare reconnections in the current observation that completely replace the magnetic flux of the pre-existing MFR are manifested as the highly dynamic motions of the hooked ribbon and the long-distance footpoint migration, which are also different from the continuous deformation and gradual drifting of the MFR footpoints as predicted by idealized 3D MHD simulations[18,34].

Although these observations were neither anticipated from the standard picture nor reproduced in numerical simulations, they must be a consequence of the 3D magnetic reconnection that is inherently built into the 3D extension of the standard model[16–18,20]. As an important topological component in the 3D model, the hooked ribbon demonstrates complex changes and motions, which reveals new details about 3D magnetic reconnections that reshape the pre-existing MFR into the CME. Such a substantial restructuring of pre-existing MFRs during eruptions would add another layer of difficulty to forecasting space weather, but may shed light on complex ejecta in interplanetary space (Supplementary Note 1.3).

Methods

Instruments and data

The AIA[43] on board the SDO[44] takes full-disk images of the Sun around the clock. The seven EUV channels, that is, 131 Å (primarily from the Fe XXI emission line, $\log T = 7.05$), 94 Å (Fe XVIII, $\log T = 6.85$), 335 Å (Fe XVI, $\log T = 6.45$), 193 Å (primarily Fe XII, $\log T = 6.2$), 211 Å (Fe XIV, $\log T = 6.3$), 171 Å (Fe IX, $\log T = 5.85$) and 304 Å (He II, $\log T = 4.7$), obtain images with a spatial resolution of 0.6″ and a temporal cadence of 12 s. Two UV channels, 1,600 Å (C IV line and continuum emission, $\log T = 5.0$) and 1,700 Å (continuum), obtain images with a temporal cadence of 24 s. AIA data are processed to level 1.5, and the heliographic maps are all rotated to 16:00 UT to correct the solar rotation.

The HMI[45] on board SDO measures the magnetic fields on the solar photosphere. We use HMI line-of-sight magnetograms to compare with heliographic observations by AIA and IRIS. To investigate the detailed magnetic configuration of the active region, we use the SHARP vector magnetograms, which are taken every 12 min and remapped with the CEA projection, with a pixel scale of about 0.36 Mm. At the PIL of the active region, which is identified by the contour of $B_z = 0$, we search for the existence of BPs (Fig. 2f) by employing the criterion $(B_\perp \cdot \nabla_\perp B_z)|_{\rm PIL} > 0$ (refs. 46,47) ($\perp$ refers to the horizontal components of the magnetic field $\mathbf{B}$ and ∇B_z), where magnetic field vectors are directed from negative to positive polarities and the field line is tangential to the photosphere and concave upward. BPs are topological structures known to be favourable for the formation of current sheets and therefore for the occurrence of magnetic reconnection (see also Supplementary Note 1.2).

IRIS[48] captures the formation and eruption phase of the event before 17:58 UT. The SJI obtains images with a 19 s cadence and a spatial resolution as high as $\frac{1}{6}$″ over an FOV of 119″ × 119″, which fortuitously covers the eastern foot of the MFR (Supplementary Video 3). IRIS level-2 data of the SJI Si IV 1,400 Å passband ($\log T \approx 4.9$, forming in the transition region) are used in the study. The superior spatiotemporal resolution of IRIS is key to this study; for example, it registers brightening in 1,400 Å around the eastern footpoint of the seed MFR as soon as it appears in EUV at 16:45 UT (Fig. 2e), suggestive of simultaneous heating in the low atmosphere. However, the brightening is too thin to be clearly resolved by AIA UV channels during this early phase. The subsequent footpoint evolution of the seed MFR is resolved by both IRIS and SDO/AIA, but the morphology and evolution of flare ribbons are better resolved by IRIS both temporally and spatially. IRIS observations hence serve as a reference and guide for our identification of flare ribbons observed by AIA. Together, IRIS and AIA observations make it possible to estimate the pre-flare reconnection rate (see below), which is rarely given in the literature.

To characterize the temporal evolution, we place four virtual slits (S1–S4; Extended Data Figs. 2 and 4) in SDO/AIA and IRIS images and generate the time–distance stack plots (Fig. 4c–f). S1 is put across the sigmoid in SDO/AIA 131 Å images (Extended Data Fig. 2a), with a length of 76 Mm, averaged over 6 AIA pixels. S2 and S3 are across the trapezoid-shaped ribbon in IRIS 1,400 Å (Extended Data Fig. 2d), with lengths of 47 and 59 Mm, respectively, averaged over 10 IRIS pixels. S4 is across the horseshoe-shaped ribbon in IRIS 1,400 Å (Extended Data Fig. 4d), with a length of 45 Mm, averaged over 10 pixels. Stack plots of S2–S4 after 17:58 UT are generated from SDO/AIA 1,600 Å images at the same locations, when there are no IRIS observations.

The GOES spacecraft operates in geosynchronous orbit and measures the solar soft X-ray flux in units of watts per square metre. The classification of solar flares uses the letters A, B, C, M or X according to the peak flux in 1–8 Å as measured by GOES, with each letter representing a 10-fold increase in flux.

DEM analysis

SDO/AIA's six optically thin EUV passbands (all except for 304 Å) are used for DEM analysis to study the temperature characteristics. The AIA data are further processed to level 1.6 before being fed into the DEM code. Here we used the sparse inversion code[49], which has been further modified to optimize solutions for hot plasmas above a few megakelvin[50]. DEMs are calculated in the temperature range of $\log T = 5.5–7.5$ with an interval of $\Delta \log T = 0.05$, and a DEM-weighted mean temperature, $\langle T\rangle = (\sum {\rm DEM}(T)\, T\, \Delta T)/(\sum {\rm DEM}(T)\, \Delta T)$, is also derived[51]. DEM uncertainties are obtained by 250 iterations of Monte Carlo simulations. We also computed the EM locus curves (${\rm EM}_\lambda(T) = I_{\rm obs}/\epsilon_\lambda(T)$) of a sampled region using the observed intensities $I_{\rm obs}$ and temperature response functions $\epsilon_\lambda(T)$ from the six AIA channels.

Identification of ribbon and coronal dimming

To characterize the ribbon evolution, we identify the low-atmosphere ribbon by counting brightened pixels in SDO/AIA UV channels (Fig. 1g) and IRIS SJI 1,400 Å passbands (Fig. 6), respectively. During the precursor phase, flare brightening in AIA 1,600 Å is too weak to be clearly distinguished from chromospheric plages, thus we use the ratio of AIA 1,600 Å and 1,700 Å passbands to enhance the ribbon brightening[30] (Extended Data Fig. 2 and Supplementary Video 3). After the flare onset at 17:21 UT, only the AIA 1,600 Å passband is used. To best identify the flare ribbons, different threshold values are set during different evolutionary phases.

The identified ribbon pixels in SDO/AIA are used to calculate the reconnection flux (Fig. 4b), after being projected onto a pre-flare SDO/HMI SHARP B_z map with the CEA projection. We measured the instantaneous reconnection flux by summing up magnetic fluxes swept by newly brightened ribbon pixels, and estimated the uncertainties by the difference of the measured magnetic flux in positive and negative polarities. Integrating the instantaneous reconnection flux with respect to time, we obtained the accumulative reconnection flux.

Compared with AIA, IRIS is superior in spatial resolution and dynamic range, though it has a limited FOV mainly covering the ribbon of negative polarity (Extended Data Figs. 2 and 4 and Supplementary Video 3). We manually traced the bright ribbon fronts observed in IRIS 1,400 Å at selected time instants to highlight the complex patterns and irregular motions (Fig. 1h).

Coronal dimmings around the ribbon NR are evident and migrate in the SDO/AIA 335 Å passband during the MFR eruption (Extended Data Fig. 4 and Supplementary Video 4). To study the dimming evolution, we identified dimmings as the pixels whose brightness decreases compared with that before the eruption (we refer to 16:20 UT for the event; Fig. 6e–h), and took the average brightness to obtain the 335 Å dimming lightcurve (Fig. 4a). For the conjugated pair of post-eruption dimmings detected at the footpoints of large-scale overlying loops (Extended Data Fig. 6d), we sampled intensities at two representative locations in SDO/AIA 171 Å ('DS' and 'DN' in Extended Data Fig. 6d, 10″ × 10″) to show their temporal evolution (Fig. 4a).

To quantitatively study the footpoint migration, we compare two time instants before and after the eruption as an illustration, when the eastern foot of the MFR is well defined: that is, at about 17:18 UT, when it is enclosed by a trapezoidal ribbon (Fig. 6a), and after 17:50 UT, when it is marked by the coronal dimming that is concentrated in the opening of the ribbon hook (see, for example, Fig. 6h). One can see that the centroid of magnetic fluxes within the foot migrates from about [−167″, 111″] to [−108″, 76″] (Fig. 6h), which is shifted by about 70″ with an average migrating speed of about 26 km s^{-1}. The magnetic flux through the foot changes from about 3.3×10^{20} Mx to 7.9×10^{20} Mx accordingly, an increase of nearly twofold. While the foot boundary is difficult to determine at other times during the eruption, the substantial displacement of the foot and the increase of magnetic flux through it strongly evidence a complete restructuring of the original MFR during its development into the CME.

Data availability

The data used in the study are publicly available for download from the corresponding mission archives. SDO data are available at http://jsoc.stanford.edu/ajax/lookdata.html; IRIS data are available at https://iris.lmsal.com/data.html.

References

1. Patsourakos, S. et al. Decoding the pre-eruptive magnetic field configurations of coronal mass ejections. *Space Sci. Rev.* **216**, 131 (2020).
2. Liu, R. Magnetic flux ropes in the solar corona: structure and evolution toward eruption. *Res. Astron. Astrophys.* **20**, 165 (2020).
3. Priest, E. R. & Forbes, T. G. The magnetic nature of solar flares. *Astron. Astrophys. Rev.* **10**, 313–377 (2002).
4. Temmer, M. Space weather: the solar perspective. *Living Rev. Sol. Phys.* **18**, 4 (2021).
5. Cheng, X., Guo, Y. & Ding, M. Origin and structures of solar eruptions I: magnetic flux rope. *Sci. China Earth Sci.* **60**, 1383–1407 (2017).
6. Schmieder, B., Aulanier, G. & Vršnak, B. Flare-CME models: an observational perspective. *Sol. Phys.* **290**, 3457–3486 (2015).
7. Green, L. M., Török, T., Vršnak, B., Manchester, W. & Veronig, A. The origin, early evolution and predictability of solar eruptions. *Space Sci. Rev.* **214**, 46 (2018).
8. Zhang, J., Cheng, X. & Ding, M.-D. Observation of an evolving magnetic flux rope before and during a solar eruption. *Nat. Commun.* **3**, 747 (2012).
9. Patsourakos, S., Vourlidas, A. & Stenborg, G. Direct evidence for a fast coronal mass ejection driven by the prior formation and subsequent destabilization of a magnetic flux rope. *Astrophys. J.* **764**, 125 (2013).
10. Moore, R. L., Sterling, A. C., Hudson, H. S. & Lemen, J. R. Onset of the magnetic explosion in solar flares and coronal mass ejections. *Astrophys. J.* **552**, 833–848 (2001).
11. Karpen, J. T., Antiochos, S. K. & DeVore, C. R. The mechanisms for the onset and explosive eruption of coronal mass ejections and eruptive flares. *Astrophys. J.* **760**, 81 (2012).
12. Gou, T., Liu, R., Kliem, B., Wang, Y. & Veronig, A. M. The birth of a coronal mass ejection. *Sci. Adv.* **5**, eaau7004 (2019).
13. Kopp, R. A. & Pneuman, G. W. Magnetic reconnection in the corona and the loop prominence phenomenon. *Sol. Phys.* **50**, 85–98 (1976).
14. Lin, J. & Forbes, T. G. Effects of reconnection on the coronal mass ejection process. *J. Geophys. Res.* **105**, 2375–2392 (2000).
15. Démoulin, P. Extending the concept of separatrices to QSLs for magnetic reconnection. *Adv. Space Res.* **37**, 1269–1282 (2006).
16. Aulanier, G., Janvier, M. & Schmieder, B. The standard flare model in three dimensions. I. Strong-to-weak shear transition in post-flare loops. *Astron. Astrophys.* **543**, A110 (2012).
17. Aulanier, G. et al. The standard flare model in three dimensions. II. Upper limit on solar flare energy. *Astron. Astrophys.* **549**, A66 (2013).
18. Janvier, M., Aulanier, G., Pariat, E. & Démoulin, P. The standard flare model in three dimensions. III. Slip-running reconnection properties. *Astron. Astrophys.* **555**, A77 (2013).
19. Titov, V. S., Hornig, G. & Démoulin, P. Theory of magnetic connectivity in the solar corona. *J. Geophys. Res. Space Phys.* **107**, 1164 (2002).
20. Janvier, M. et al. Electric currents in flare ribbons: observations and three-dimensional Standard Model. *Astrophys. J.* **788**, 60 (2014).
21. Wang, W. et al. Buildup of a highly twisted magnetic flux rope during a solar eruption. *Nat. Commun.* **8**, 1330 (2017).
22. Veronig, A. M., Gömöry, P., Dissauer, K., Temmer, M. & Vanninathan, K. Spectroscopy and differential emission measure diagnostics of a coronal dimming associated with a fast halo CME. *Astrophys. J.* **879**, 85 (2019).
23. Xing, C., Cheng, X. & Ding, M. D. Evolution of the toroidal flux of CME flux ropes during eruption. *Innovation* **1**, 100059 (2020).
24. Burlaga, L., Sittler, E., Mariani, F. & Schwenn, R. Magnetic loop behind an interplanetary shock: Voyager, Helios, and IMP 8 observations. *J. Geophys. Res.* **86**, 6673–6684 (1981).
25. Klein, L. W. & Burlaga, L. F. Interplanetary magnetic clouds at 1 AU. *J. Geophys. Res.* **87**, 613–624 (1982).
26. Chi, Y. et al. Statistical study of the interplanetary coronal mass ejections from 1995 to 2015. *Sol. Phys.* **291**, 2419–2439 (2016).
27. Vourlidas, A., Lynch, B. J., Howard, R. A. & Li, Y. How many CMEs have flux ropes? Deciphering the signatures of shocks, flux ropes, and prominences in coronagraph observations of CMEs. *Sol. Phys.* **284**, 179–201 (2013).
28. Song, H. Q. et al. Do all interplanetary coronal mass ejections have a magnetic flux rope structure near 1 au? *Astrophys. J. Lett.* **901**, L21 (2020).
29. Cheng, X., Ding, M. D. & Fang, C. Imaging and spectroscopic diagnostics on the formation of two magnetic flux ropes revealed by SDO/AIA and IRIS. *Astrophys. J.* **804**, 82 (2015).
30. Dudík, J. et al. Slipping magnetic reconnection, chromospheric evaporation, implosion, and precursors in the 2014 September 10 X1.6-class solar flare. *Astrophys. J.* **823**, 41 (2016).
31. Zhao, J. et al. Hooked flare ribbons and flux-rope-related QSL footprints. *Astrophys. J.* **823**, 62 (2016).
32. Démoulin, P., Priest, E. R. & Lonie, D. P. Three-dimensional magnetic reconnection without null points 2. Application to twisted flux tubes. *J. Geophys. Res.* **101**, 7631–7646 (1996).
33. Li, T. & Zhang, J. Quasi-periodic slipping magnetic reconnection during an X-class solar flare observed by the Solar Dynamics Observatory and Interface Region Imaging Spectrograph. *Astrophys. J. Lett.* **804**, L8 (2015).
34. Aulanier, G. & Dudík, J. Drifting of the line-tied footpoints of CME flux-ropes. *Astron. Astrophys.* **621**, A72 (2019).
35. Dudík, J., Lörinčík, J., Aulanier, G., Zemanová, A. & Schmieder, B. Observation of all pre- and post-reconnection structures involved in three-dimensional reconnection geometries in solar eruptions. *Astrophys. J.* **887**, 71 (2019).
36. van Driel-Gesztelyi, L. et al. Coronal magnetic reconnection driven by CME expansion—the 2011 June 7 event. *Astrophys. J.* **788**, 85 (2014).
37. Török, T. et al. Sun-to-Earth MHD simulation of the 2000 July 14 'Bastille Day' eruption. *Astrophys. J.* **856**, 75 (2018).
38. Qiu, J., Hu, Q., Howard, T. A. & Yurchyshyn, V. B. On the magnetic flux budget in low-corona magnetic reconnection and interplanetary coronal mass ejections. *Astrophys. J.* **659**, 758–772 (2007).
39. Wang, Y., Zhou, Z., Shen, C., Liu, R. & Wang, S. Investigating plasma motion of magnetic clouds at 1 AU through a velocity-modified cylindrical force-free flux rope model. *J. Geophys. Res. Space Phys.* **120**, 1543–1565 (2015).
40. Kazachenko, M. D., Lynch, B. J., Welsch, B. T. & Sun, X. A database of flare ribbon properties from the Solar Dynamics Observatory. I. Reconnection flux. *Astrophys. J.* **845**, 49 (2017).

41. Tschernitz, J., Veronig, A. M., Thalmann, J. K., Hinterreiter, J. & Pötzi, W. Reconnection fluxes in eruptive and confined flares and implications for superflares on the Sun. *Astrophys. J.* **853**, 41 (2018).
42. Jiang, C. et al. A fundamental mechanism of solar eruption initiation. *Nat. Astron.* **5**, 1126–1138 (2021).
43. Lemen, J. R. et al. The Atmospheric Imaging Assembly (AIA) on the Solar Dynamics Observatory (SDO). *Sol. Phys.* **275**, 17–40 (2012).
44. Pesnell, W. D., Thompson, B. J. & Chamberlin, P. C. The Solar Dynamics Observatory (SDO). *Sol. Phys.* **275**, 3–15 (2012).
45. Schou, J. et al. Design and ground calibration of the Helioseismic and Magnetic Imager (HMI) instrument on the Solar Dynamics Observatory (SDO). *Sol. Phys.* **275**, 229–259 (2012).
46. Titov, V. S., Priest, E. R. & Demoulin, P. Conditions for the appearance of 'bald patches' at the solar surface. *Astron. Astrophys.* **276**, 564–570 (1993).
47. Titov, V. S. & Démoulin, P. Basic topology of twisted magnetic configurations in solar flares. *Astron. Astrophys.* **351**, 707–720 (1999).
48. De Pontieu, B. et al. The Interface Region Imaging Spectrograph (IRIS). *Sol. Phys.* **289**, 2733–2779 (2014).
49. Cheung, M. C. M. et al. Thermal diagnostics with the Atmospheric Imaging Assembly on board the Solar Dynamics Observatory: a validated method for differential emission measure inversions. *Astrophys. J.* **807**, 143 (2015).
50. Su, Y. et al. Determination of differential emission measure from solar extreme ultraviolet images. *Astrophys. J. Lett.* **856**, L17 (2018).
51. Gou, T., Liu, R. & Wang, Y. Do all candle-flame-shaped flares have the same temperature distribution? *Sol. Phys.* **290**, 2211–2230 (2015).

Acknowledgements

We acknowledge SDO and IRIS teams for the science data. IRIS is a NASA Small Explorer Mission developed and operated by LMSAL with mission operations executed at NASA Ames Research Center and major contributions to downlink communications funded by ESA and the Norwegian Space Centre. T.G. thanks the BBSO staff for providing Hα data. T.G., R.L., W.W., M.X. and Y.M. acknowledge support from the National Natural Science Foundation of China (NSFC 42188101, 42274204, 11903032, 11925302, 12003032) and the Strategic Priority Program of the Chinese Academy of Sciences (XDB41030100). A.M.V. acknowledges the Austria Science Fund (FWF), project I-4555N. T.L. acknowledges support from NSFC 12222306. T.G. also acknowledges support from the CAS Key Laboratory of Solar Activity.

Author contributions

T.G. and R.L. led the study and analysis, interpreted the data, and wrote the manuscript. A.M.V. discussed the analysis and contributed to the interpretation, conclusion, and writing of the manuscript. B.Z. led the in situ data analysis and discussed the interpretation. T.L. and Y.W. discussed the results and contributed to the interpretation. W.W. and M.X. contributed to the SDO and in situ data analyses. All authors participated in the discussion and contributed to finalizing the manuscript.

Competing interests

The authors declare no competing interests.

Additional information

Extended data is available for this paper at https://doi.org/10.1038/s41550-023-01966-2.

Supplementary information The online version contains supplementary material available at https://doi.org/10.1038/s41550-023-01966-2.

Correspondence and requests for materials should be addressed to Tingyu Gou or Rui Liu.

Peer review information *Nature Astronomy* thanks Hongqiang Song and the other, anonymous, reviewer(s) for their contribution to the peer review of this work.

https://doi.org/10.1038/s41550-023-01966-2

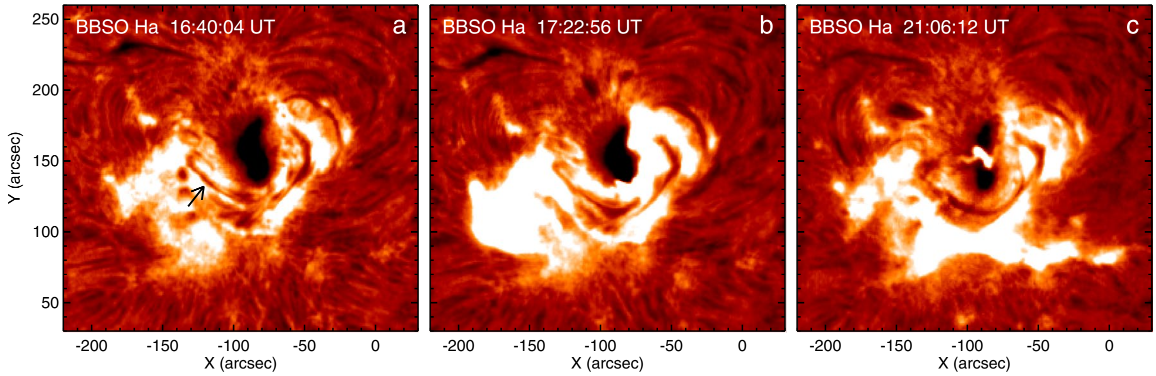

Extended Data Fig. 1 | Hα observation of the filament from the Big Bear Solar Observatory (BBSO). Panels (a-c) show the Hα line center images before, during, and after the sigmoid eruption, respectively. The arrow in panel (a) denotes the filament aligned with the main PIL of the active region.

https://doi.org/10.1038/s41550-023-01966-2

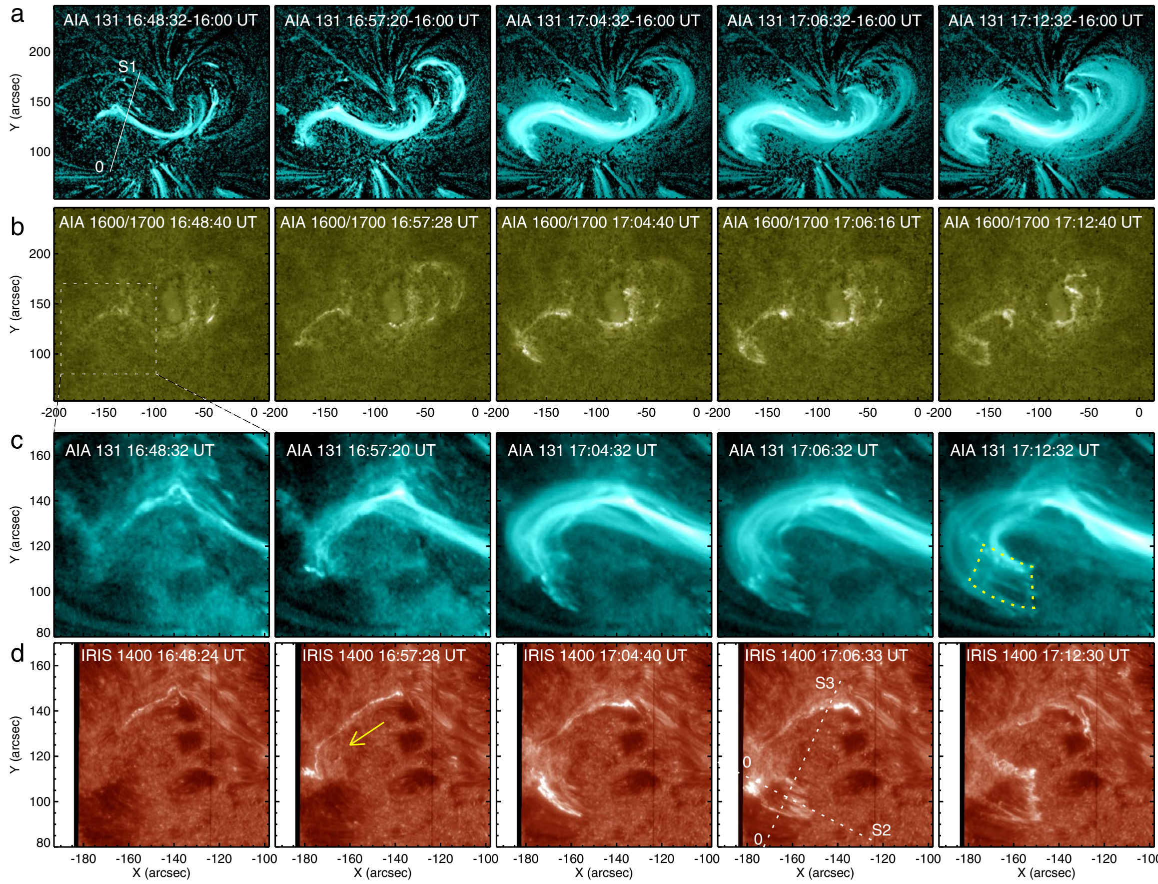

Extended Data Fig. 2 | MFR buildup during the flare precursor phase. From the top to bottom are SDO/AIA 131 Å base-difference images, ratio of SDO/AIA 1600 Å and 1700 Å images, SDO/AIA 131 Å images zooming in on the eastern foot of the sigmoid, and simultaneous IRIS SJI 1400 Å images (Methods). The white dotted rectangle in panel (b) indicates the FOV of panels (c & d). Three white lines in panels (a & d) indicate the virtual slits S1-S3 for the stack plots in Fig. 4(c–e) (Methods), whose starting points are labeled as '0'. The yellow arrow in the IRIS image indicates the extending direction of the ribbon. Yellow dotted lines in the AIA 131 Å image at 17:12 UT denote the location of the trapezoidal ribbon observed in IRIS 1400 Å at the same time (see also Fig. 5a & d).

https://doi.org/10.1038/s41550-023-01966-2

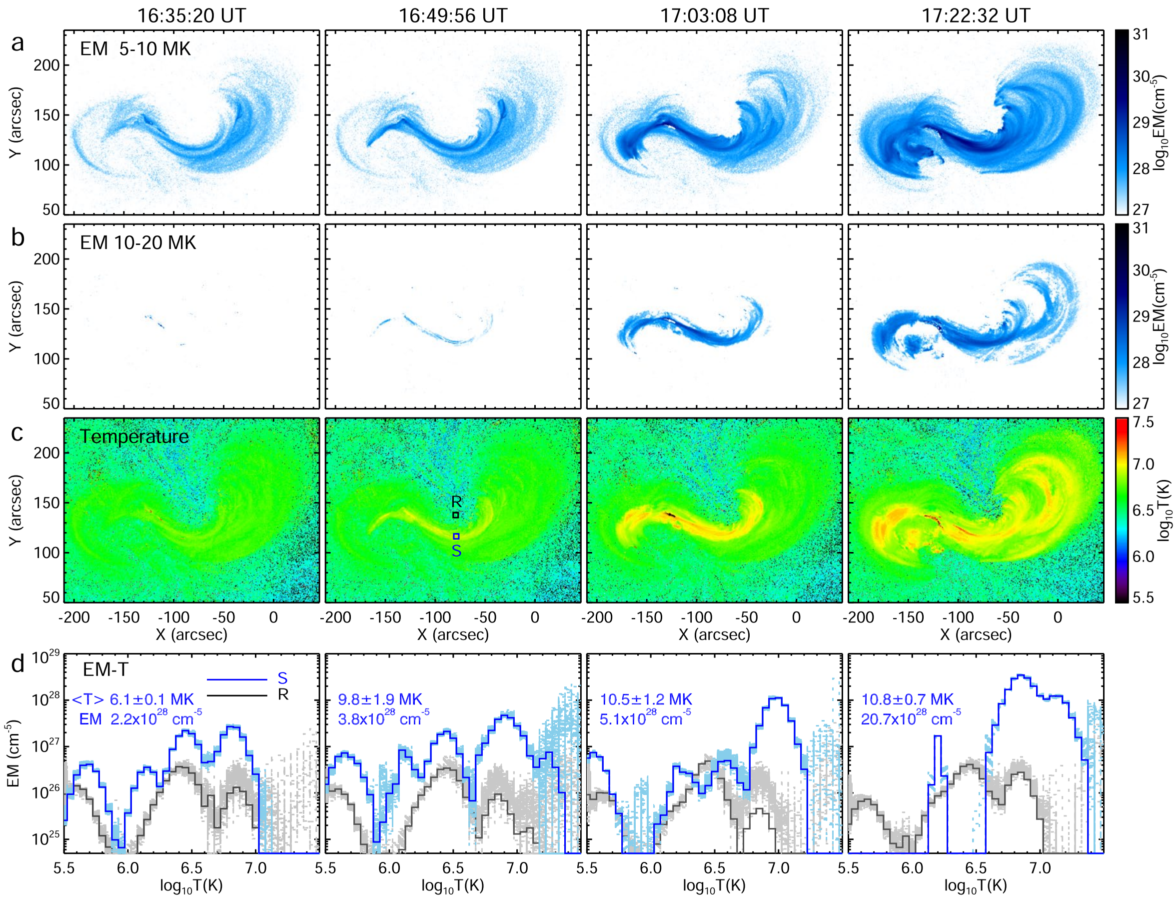

Extended Data Fig. 3 | DEM results in different evolutionary phases. (a,b) EM maps in temperature ranges of 5-10 and 10-20 MK, respectively. (c) Maps of the DEM-weighted mean temperature (Methods). (d) DEM distributions sampled from two locations (4 × 4 pixels^2), one on the sigmoid ('S') and the other from nearby as a reference ('R'), in blue and black, respectively. Light blue and gray curves give 250 times of Monte Carlo simulations as an estimation of the DEM uncertainty (Methods). The mean temperature and total EM of the sigmoid sample 'S' are annotated.

https://doi.org/10.1038/s41550-023-01966-2

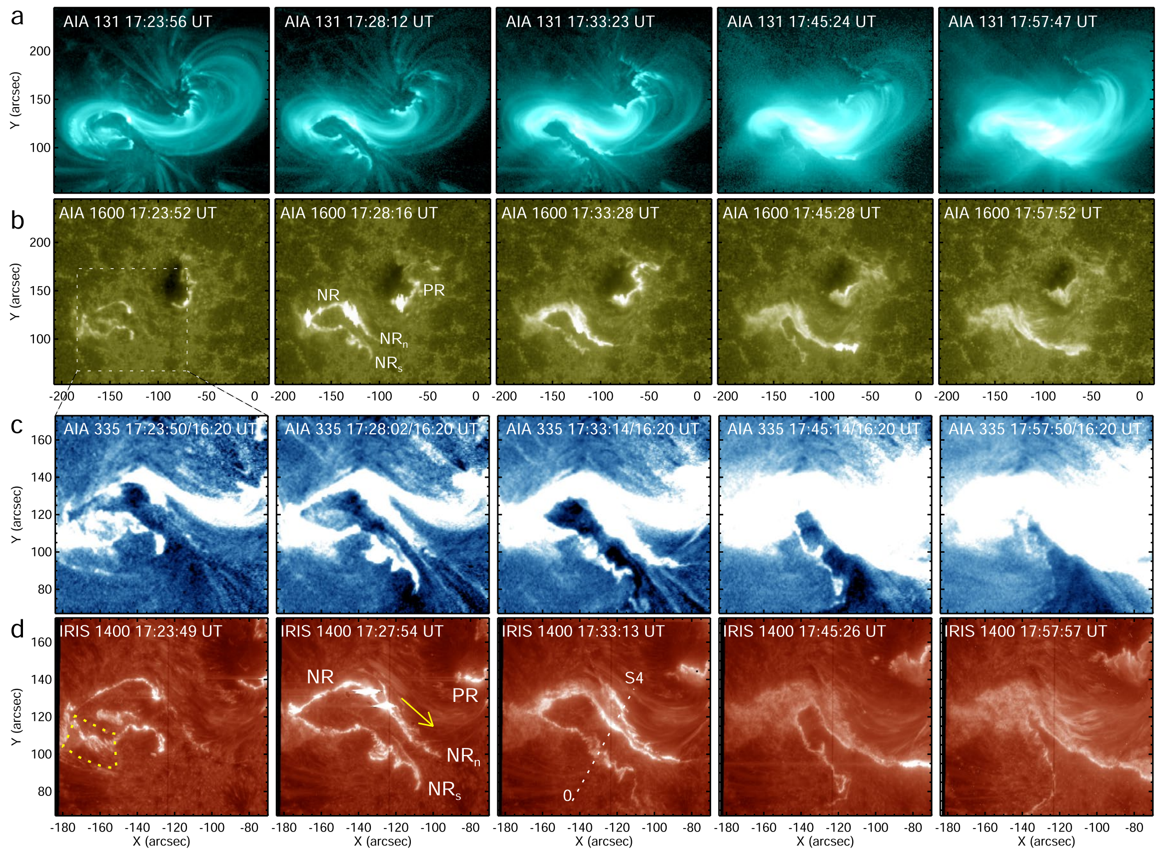

Extended Data Fig. 4 | SDO/AIA and IRIS observations during the MFR eruption phase. From the top to bottom are SDO/AIA 131 Å, 1600 Å, 335 Å base ratio, and IRIS SJI 1400 Å images. The white dotted rectangle in panel (b) indicates the FOV of panels (c & d). The yellow dotted lines in IRIS 1400 Å are the same as those in Fig. 5 & Extended Data Fig. 2. The yellow arrow indicates the extending direction of the negative ribbon NR$_n$. The white dotted line indicates the virtual slit S4 for the stack plot in Fig. 4f (Methods), with its starting point labeled by '0'.

https://doi.org/10.1038/s41550-023-01966-2

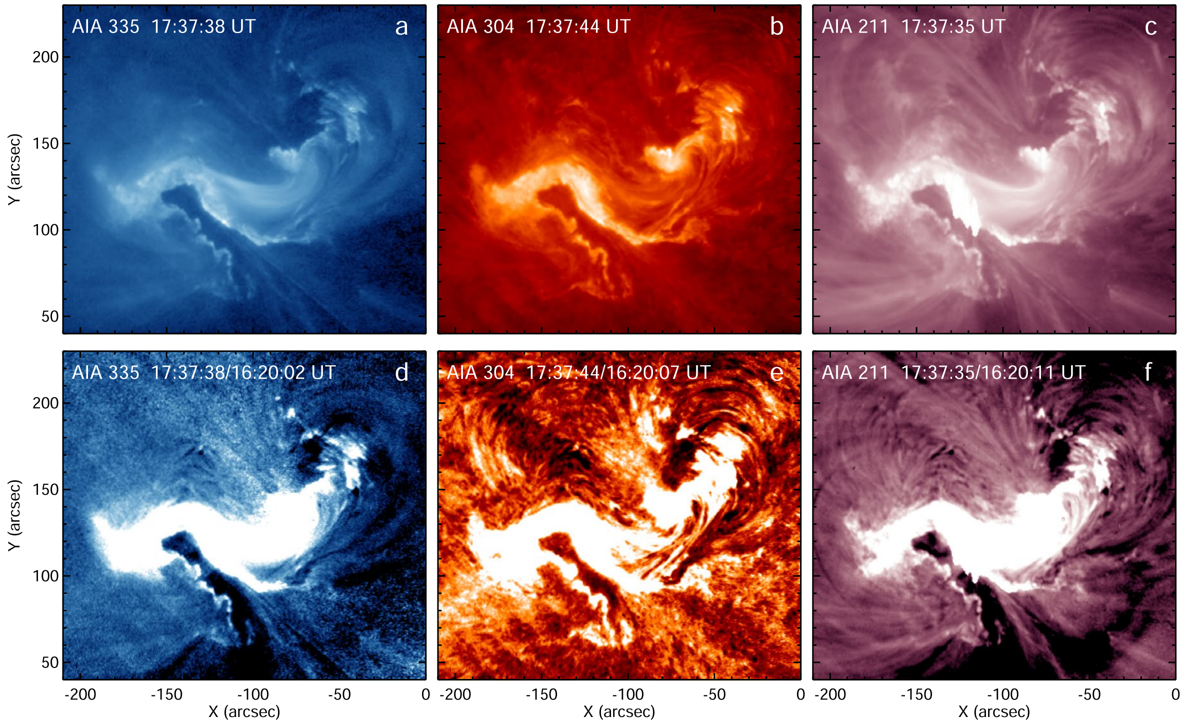

Extended Data Fig. 5 | Coronal dimmings during the MFR eruption. Panels (a-c) show the SDO/AIA 335 Å, 304 Å, and 211 Å images, and panels (d-f) show corresponding base-ratio images.

https://doi.org/10.1038/s41550-023-01966-2

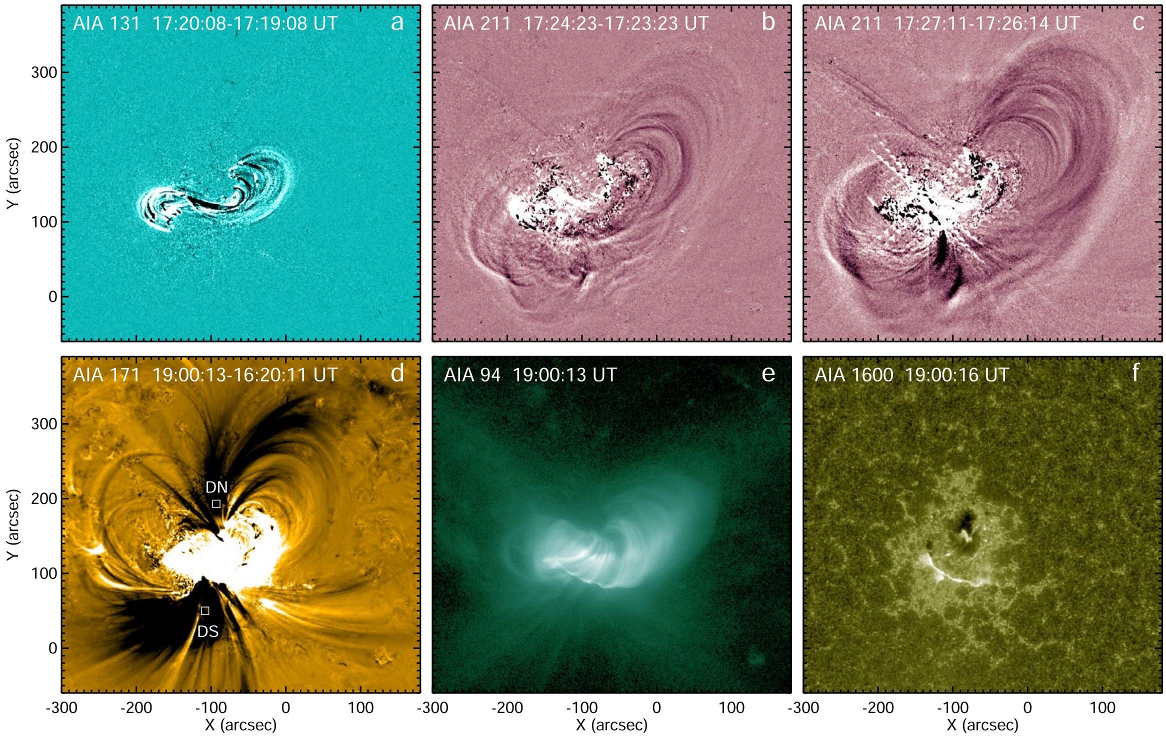

Extended Data Fig. 6 | SDO/AIA observations of the sigmoid eruption. (a-c) AIA 131 Å and 211 Å running-difference images showing the pre-eruption MFR and the erupting CME. (d-f) AIA observations of coronal dimmings in 171 Å base-difference image, post-flare loops in 94 Å, and flare ribbons in 1600 Å, during the flare decay phase. Two boxes in panel (d) indicate the regions to obtain 171 Å dimming lightcurves in Fig. 4a (Methods).